# Comparing Rate and Mechanism of Ethane Hydrogenolysis on Transition-Metal Catalysts

Abdulrahman Almithn and David Hibbitts[*]

Department of Chemical Engineering, University of Florida, Gainesville, Florida 32611, United States

S *Supporting Information*

ABSTRACT: The effects of metal catalyst identity on the ethane hydrogenolysis rates and mechanism were examined using density functional theory (DFT) for Group 8−11 metals (Ru, Os, Rh, Ir, Ni, Pd, Pt, Cu, Ag, and Au). Previously measured turnover rates on Ru, Rh, and Ir clusters show H_2-pressure dependence of $[H_2]^{-3}$, consistent with C−C bond activation in *CHCH* intermediates in reactions that require two H* (chemisorbed H) to desorb from the H*-covered surfaces that prevail at these hydrogenolysis conditions. Previous DFT calculations on Ir catalysts have shown that C−C bonds in alkanes are weakened by forming C−metal bonds through quasi-equilibrated dehydrogenation steps

during ethane hydrogenolysis, and these steps form *CHCH* intermediates which undergo a kinetically relevant C−C bond cleavage step. Here, the DFT-calculated free-energy barriers show that *CH−CH* bond activation is also more favorable than all C−C bond activations in other intermediates on Group 8−10 metals by >34 kJ mol^{-1} with the exception of Pd, where *CHCH* and CH$_3$CH* activate with similar activation free energies (242 and 253 kJ mol^{-1}, respectively, 593 K). The relative free-energy barriers between *CH−CH* bond cleavage and C−C bond cleavage in more saturated intermediates decrease as one moves from left to right in the periodic table until *CH$_3$−CH$_2$* bond cleavage becomes more favorable on Group 11 coinage metals (Cu, Ag, and Au). Such predicted trends are consistent with the measured turnover rates that decrease as Ru > Rh > Ir > Pt and show H_2-pressure dependence of $\sim[H_2]^{-3}$ ($\lambda = 3$) for Ru, Rh, and Ir clusters and $[H_2]^{-2.3}$ ($\lambda = 2.3$) for Pt clusters. The decrease in the measured λ value for Pt, however, is caused by a decrease in the number of desorbed H* atoms from the surface ($\gamma = 0−1$) rather than a change in the mechanism as shown here using a H*-covered Pt$_{119}$ half-particle model. The lower H*-coverage on Pt compared to other metals and the lateral relaxation of the adlayer in curved nanoparticle models, as reported previously, allow *CH−CH* bond cleavage to occur at a lower number of vacant sites on Pt.
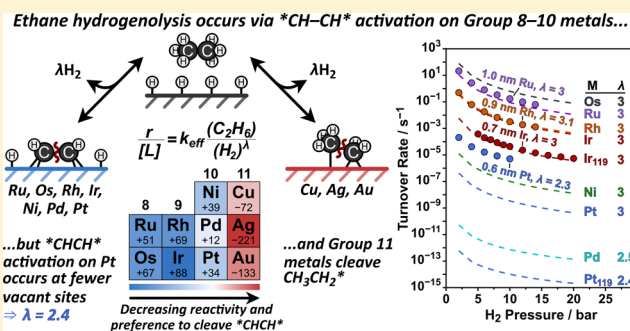
1. INTRODUCTION

Catalytic alkane hydrogenolysis on transition-metal surfaces is used to decrease the chain length of acyclic alkanes and produce branched alkanes, thus increasing the octane number of fuel.[1−7] Hydrogenolysis is also an undesired side reaction in hydrocarbon reforming and isomerization processes;[8−10] therefore, understanding the mechanism and selectivity of alkane hydrogenolysis on metal catalysts is crucial for optimal operation. Broadly speaking, understanding the role of H$_2$, the degree of unsaturation, and the role of branching during C−C bond hydrogenolysis reactions informs related chemistry in the selective and complete hydrogenolysis of C−O,[11−14] C−S,[15−17] and C−N bonds[18,19] in various applications relevant to biorenewable and conventional feedstock processing and upgrading.

Previous studies have shown that weakening the C−C bond in *n*-alkanes (C$_2$−C$_{10}$),[20−30] branched alkanes (C$_4$−C$_6$),[28,31−33] and alkyl cyclohexanes[31,34] occurs through a series of quasi-equilibrated dehydrogenation steps that form unsaturated species bound to the metal surface which eventually undergo C−C bond cleavage.[20−23,27,31,32,34] The

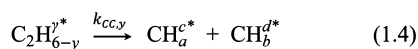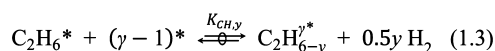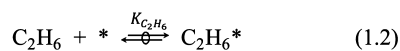formation of H$_2$(g) during these dehydrogenation and H* desorption steps also increases reaction rates by increasing the activation entropies and, consequently, decreasing the activation free energies. Density functional theory (DFT) calculations have been used, in concert with high-pressure kinetics, to determine the identity and structure of these unsaturated species that undergo C−C bond cleavage.[23,27,32,35] However, these DFT studies have focused on Ir catalysts, and therefore, the effects of the metal catalyst identity on the alkane hydrogenolysis mechanism remain unknown.

Scheme 1 shows a sequence of elementary steps for ethane hydrogenolysis, which are analogous to steps for *n*-alkanes (C$_2$−C$_{10}$),[20−30] branched alkanes (C$_4$−C$_6$),[28,31−33] and alkyl cyclohexane.[31,34] Dissociative H$_2$ adsorption (Step 1.1) and ethane adsorption (1.2) are followed by a series of quasi-equilibrated dehydrogenation steps (1.3) to form partially dehydrogenated intermediates (C$_2$H$_{6-y}^{\gamma*}$). The observed equi-

Scheme 1. Proposed Mechanism for Ethane Hydrogenolysis on Metal Catalysts[22,23a]

$$H_2 + 2* \underset{K_{H_2}}{\overset{\ominus}{\rightleftharpoons}} 2H* \qquad (1.1)$$

$$C_2H_6 + * \underset{K_{C_2H_6}}{\overset{\ominus}{\rightleftharpoons}} C_2H_6* \qquad (1.2)$$

$$C_2H_6* + (\gamma - 1)* \underset{K_{CH,y}}{\overset{\ominus}{\rightleftharpoons}} C_2H_{6-y}^{\gamma*} + 0.5y\,H_2 \quad (1.3)$$

$$C_2H_{6-y}^{\gamma*} \xrightarrow{k_{CC,y}} CH_a^{c*} + CH_b^{d*} \qquad (1.4)$$

$$CH_a^{c*} + xH* \underset{K_{CH_4}}{\overset{\ominus}{\rightleftharpoons}} CH_4 + (x+c)* \qquad (1.5)$$

[a]The double arrow with an overlaid circle indicates a quasi-equilibrated reaction, * indicates a vacant site on a H*-covered surface, $\gamma*$ indicates an adsorbate occupying a γ vacant site, and K_x and k_x are equilibrium and rate constants for individual steps, respectively. Reprinted from ref 35.

librated mixtures of alkane–alkene and cyclohexane–arene during alkane hydrogenolysis on Ir, Pt, Ru, and Rh catalysts[22,23,31,34] indicate that steps 1.1−1.3 are indeed quasi-equilibrated. The kinetically relevant C−C bond cleavage step (1.4) then occurs via these unsaturated intermediates at a rate described by

$$\frac{r_y}{[L]} = k_{CC,y} \frac{(\prod_{i=1}^{y} K_{CH,i})\, K_{C_2H_6}(C_2H_6)}{K_{H_2}(H_2)^{\lambda}} \qquad (1)$$

at high H_2/alkane ratios where chemisorbed hydrogen (H*) covers the metal surface. The $(\prod_{i=1}^{y} K_{CH,i})$ term represents the product of the equilibrium constants for the y C−H activation steps before C−C bond cleavage, and λ is the number of $H_2(g)$ molecules evolved as a result of y dehydrogenation steps and γ H* atoms desorbed from the H*-covered surface (to accommodate the transition state) such that

$$\lambda = 1/2\,(y + \gamma) \qquad (2)$$

Previously measured ethane hydrogenolysis rates (0.2 bar ethane, 2−20 bar H_2, 593 K) showed that λ had values of 3.3 on 7 nm Ir[23] and 3.0 on 0.7 nm Ir,[22] indicating a small impact of particle size. Additional experiments on other catalysts yielded λ values of 3.1 on Rh (0.9 nm) and 3.0 on Ru (1.0 nm).[22,31] Ethane hydrogenolysis on Pt gave a λ value of 2.3 on 0.6 nm clusters,[22] significantly lower than the values near 3 on Ir, Rh, and Ru catalysts. These measurements give the total amount of H_2 formed during the formation of the kinetically relevant C−C activation transition state (Step 1.4 in Scheme 1); they cannot, however, determine the amount of H_2 formed via quasi-equilibrated C−H activation steps of the alkane (y) or the amount of H_2 formed via H* removal from H*-covered surfaces (γ) independently. DFT calculations of ethane hydrogenolysis on bare Ir(111) surface models demonstrated that ethane hydrogenolysis occurs predominantly via the *CHCH* reactive intermediate ($y = 4$);[23] assuming that the reaction requires two sites ($\gamma = 2$), C−C bond cleavage in *CHCH* gives a λ value of 3 (eq 2), in agreement with the measured values.[22,23] More recently, we confirmed that this reaction requires two sites (follows 2 H* desorption steps) by modeling the reaction on a H*-covered Ir_{119} half-particle model that accounts for coadsorbate interactions and accurately predicts turnover rates and H_2-pressure dependence (λ).[35]

The consistency of measured λ values (∼3) for ethane hydrogenolysis across different metals (Ir, Rh, and Ru) suggests that the ethane hydrogenolysis mechanism on Rh and Ru is similar to that on Ir (cleaving the C−C bond via *CHCH* intermediate). The lower measured λ value on 0.6 nm Pt (∼2.3), however, indicates that either fewer H-atoms are removed from the alkane reagent (i.e., C−C bonds cleave in $C_2H_{6-y}^*$ species where $y < 4$) or that Pt also cleaves the C−C bond via the *CHCH* intermediate but requires fewer H* atoms to be desorbed from the H*-covered surface ($\gamma < 2$, eq 2). Previous H_2 chemisorption measurements and DFT studies showed that Pt saturates at lower H* coverages than Ir;[36−38] for example, a 1.0 nm Pt particle saturates at 1.75 ML compared to 2.4 ML for an Ir particle of similar size.[38] As a result, coadsorbate interactions are weaker on Pt, allowing the C−C bond cleavage to occur after fewer H* atoms desorb from the surface. Here, we examine ethane hydrogenolysis on Pt and other transition-metal surfaces using DFT to investigate the effects of metal identity on the reaction mechanism.

2. COMPUTATIONAL METHODS

Periodic, planewave DFT calculations were performed using the Vienna Ab initio Simulation Package.[39−42] Planewaves were constructed using projector augmented-wave potentials with an energy cutoff of 396 eV.[43,44] The revised Perdew−Burke−Ernzerhof (RPBE) form of the generalized gradient approximation was used to describe exchange and correlation energies.[45−47] Wavefunctions were converged until electronic energies varied less than 10^{-6} eV. Forces on all atoms were determined using a fast Fourier transform grid with a cutoff equal to twice the planewave cutoff, and structures were geometrically optimized until the forces on all atoms were less than 0.05 eV Å^{-1}. Gas-phase calculations of C_2H_6 and H_2 were modeled within an $18 \times 18 \times 18$ Å unit cell of empty space, and the Brillouin zone for such calculations was sampled at the Γ-point.

The metal (111) surfaces for FCC metals and (001) surfaces for HCP metals (Ru and Os) were modeled as 3×3 periodic lattices with four layers orthogonal to the surface and 10 Å of vacuum separating slabs (Figure 1a,c); the bottom two layers were fixed in their bulk positions, and the top two layers were relaxed. A $4 \times 4 \times 1$ Monkhorst−Pack sampling of the first Brillouin zone (k-point mesh)[48,49] was used during geometric convergence, and after geometric convergence, a single-point calculation with an $8 \times 8 \times 1$ k-point mesh was performed to determine the electronic energy. Ni(111) surface calculations were run spin-polarized because of its ferromagnetic properties. Additional calculations discussed in Section 3.3 were carried out using a H*-covered Pt_{119} hemispherical particle (Figure 1b,d) derived from a Pt_{201} cubo-octahedral particle (1.6 nm in diameter) as described in our previous study.[35] This model has a H* coverage of 1.3 ML, consistent with the previously reported saturation coverage for this particle size.[38] The bottom two layers of the hemispherical particle and the H* atoms bound to them were kept fixed at their positions in the full particle and the top two layers were relaxed. The Brillouin zone was sampled only at the Γ-point for all particle calculations.
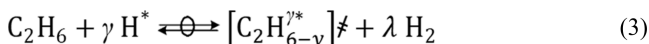
Transition-state structures for each elementary reaction were obtained by combining the nudged elastic band (NEB)[50,51] and dimer[52] methods. The NEB method was carried out using 16 images, and the wavefunctions were converged to within 10^{-4} eV. The maximum force on each atom was converged to
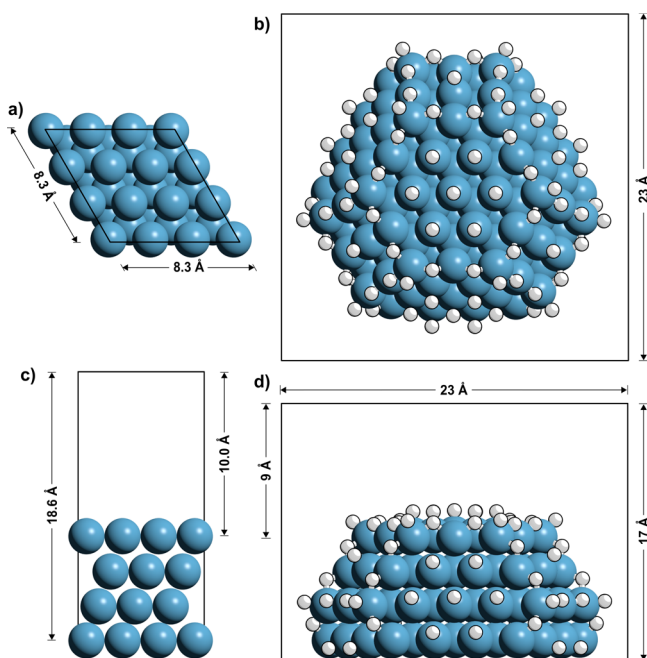
Figure 1. Top and side views of the metal 3 × 3 (111) surface (a,c) and the H*-covered Pt$_{119}$ hemispherical particle (b,d). The bottom two layers of the M(111) surface were fixed at their bulk positions during geometric convergence. The bottom two layers of the Pt$_{119}$ hemispherical particle and all H* bound to them were fixed in their Pt$_{201}$ positions during geometric convergence. All atoms except the adsorbed species and H* on the top (111) terrace were constrained during frequency calculations.

<0.5 eV Å^{-1}. These convergence criteria provided an estimate of the reaction path and initial transition-state structures and reaction modes. The dimer algorithm was then used with wavefunctions converged to within 10^{-6} eV, and the maximum force on each atom was converged to <0.05 eV Å^{-1}, consistent with all minima optimizations. Frequency calculations were performed on gas-phase molecules and all optimized adsorbed species to determine zero-point vibrational energies and vibrational, translational, and rotational enthalpy and free energy. These terms were then used, together with electronic energies (E_0, provided by VASP), to estimate enthalpies (H) and free energies (G) for reactants, products, and transition states at 593 K (the temperature at which ethane hydrogenolysis rates were measured[22,23]).

The formalism of transition-state theory[53] and the quasi-equilibrated nature of steps 1.1–1.3 in Scheme 1 dictate that gas-phase ethane and γ H* atoms are quasi-equilibrated with the C–C bond cleavage transition state ($[C_2H^{\gamma*}_{6-y}]^{\ddagger}$) and the product H$_2$

$$C_2H_6 + \gamma H^* \xrightleftharpoons[K^{\ddagger}] {} [C_2H^{\gamma*}_{6-y}]^{\ddagger} + \lambda H_2 \qquad (3)$$

where $K^{\ddagger}$ is the equilibrium constant for the formation of the transition state from gas-phase ethane and a H*-covered surface. The ethane hydrogenolysis turnover rate is related to the activation free energy ($\Delta G^{\ddagger}$) by

$$\frac{r_y}{[L]} = \frac{k_B T}{h} \exp\left(\frac{-\Delta G^{\ddagger}}{RT}\right) \frac{(C_2H_6)}{(H_2)^{\lambda}} \qquad (4)$$

here, $\Delta G^{\ddagger}$ is defined as the free energy of forming the transition state from a H*-covered surface

$$\Delta G^{\ddagger} = G[C_2H^{\gamma*\ddagger}_{6-y}] + \lambda\, G[H_2(g)] - G[\gamma H^*] \\ - G[C_2H_6(g)] \qquad (5)$$

which can be rewritten as the sum of two free-energy differences

$$\Delta G^{\ddagger} = \Delta G_k + \Delta G_\gamma \qquad (6)$$

where ΔG_k is the free energy to form the transition state on a bare metal surface

$$\Delta G_k = G[C_2H^{\gamma*\ddagger}_{6-y}] + 0.5y\, G[H_2(g)] - G[*] \\ - G[C_2H_6(g)] \qquad (7)$$

and ΔG_γ is the free energy required to desorb γ H* atoms from a H*-covered surface

$$\Delta G_\gamma = G[*] + 0.5\gamma\, G[H_2(g)] - G[\gamma H^*] \qquad (8)$$

Analogous equations for $\Delta H^{\ddagger}$ and $\Delta S^{\ddagger}$ exist through their relation to $\Delta G^{\ddagger}$

$$\Delta G^{\ddagger} = \Delta H^{\ddagger} - T\Delta S^{\ddagger} \qquad (9)$$

The DFT-predicted entropies of adsorbed H* ($S[H^*]$) using the traditional harmonic oscillator are significantly underestimated, as previously reported,[54−57] and thus, the $S[H^*]$ values were adjusted to give ΔG_γ values consistent with high H* coverages at typical hydrogenolysis conditions (Tables S1−S3, Supporting Information). These adjustments are discussed in detail in the Supporting Information (Section S2) and in Section 3.4. Further details of the computational methods can be found in the Supporting Information (Section S1).

3. RESULTS AND DISCUSSION

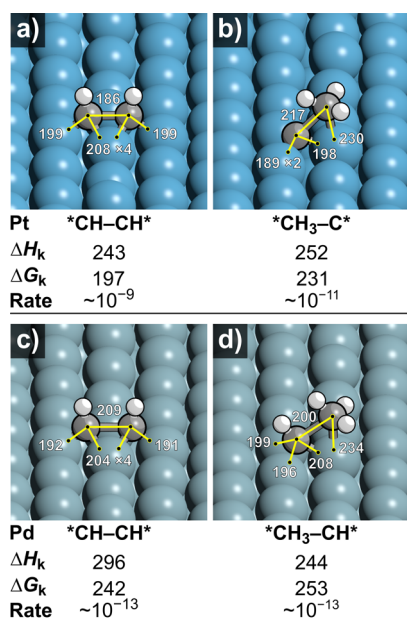### 3.1. C–C Bond Cleavage on Bare Metal Surfaces.
Calculated activation and reaction enthalpies (593 K) for elementary steps described in Scheme 1 are shown in Figure 2 for ethane hydrogenolysis on a Pt(111) surface. Desorbing two
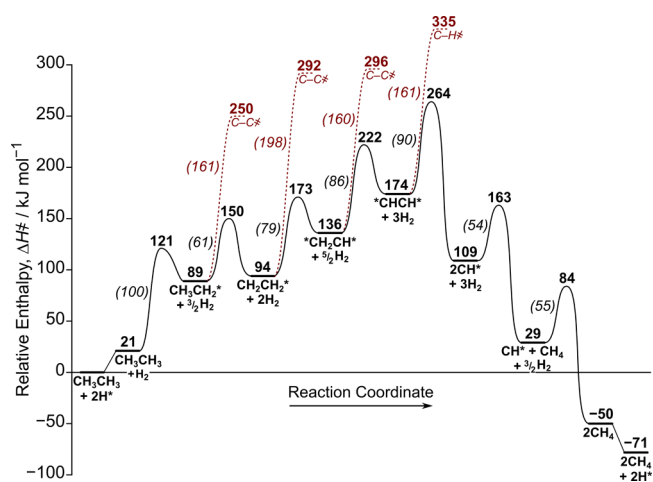
Figure 2. DFT-predicted reaction enthalpy diagram for ethane hydrogenolysis on a Pt(111) surface at 593 K. The red dashed lines show unfavorable C–C and C–H bond activation barriers. Energies relative to the H*-covered surface are shown in bold. Italicized energy values in parentheses represent intrinsic barriers. Similar diagrams for Ru, Os, Rh, Ir, Ni, Pd, Cu, Ag, and Au are shown in the Supporting Information (Figures S1−S9).

H* atoms to create two vacant sites ($\gamma = 2$) requires 21 kJ mol^{-1} on a H*-covered surface, typical at practical hydrogenolysis conditions (2−20 bar H$_2$, 0.1−0.8 bar C$_2$H$_6$, 593 K). Physisorbed C$_2$H$_6$ reacts with these two vacant sites and undergoes C−H bond activation with an enthalpic barrier of 121 kJ mol^{-1} to form CH$_3$CH$_2$* and H*. This H* atom then desorbs to maintain two vacant sites on the catalyst surface, as required for subsequent C−C or C−H bond cleavage reactions. The C−C bond in CH$_3$CH$_2$* can then cleave (to form CH$_3$* and CH$_2$*) with a barrier of 250 kJ mol^{-1}, but the C−H bond activation of CH$_3$CH$_2$* (to form *CH$_2$CH$_2$*) requires a significantly lower barrier (150 kJ mol^{-1}), as does the hydrogenation to re-form CH$_3$CH$_3$ (30 kJ mol^{-1}), confirming the quasi-equilibrated nature of these C−H activation steps. Subsequent C−H bond activations in *CH$_2$CH$_2$* and *CH$_2$CH* intermediates are also more favorable than C−C bond ruptures by at least 74 kJ mol^{-1}. After each C−H bond activation, the formed H* is desorbed to maintain two vacant sites on the surface and a constant H*-coverage during the reaction as dissociative H$_2$ adsorption is quasi-equilibrated (Scheme 1). The activation of the C−C bond in *CHCH* has a much lower intrinsic barrier (90 kJ mol^{-1}) than its dehydrogenation to form *CHC* (161 kJ mol^{-1}), indicating that ethane hydrogenolysis occurs predominantly via the *CHCH* intermediate (Figure 3a) on Pt. The

nm Pt clusters indicate that either (i) C−C bonds activate in more hydrogenated intermediates instead of *CHCH* or that (ii) fewer than two H* must be removed from the H*-covered surfaces to accommodate the *CHCH* activation reaction. These possibilities will be further examined here.

Next, we examine the enthalpy (ΔH_k) and free-energy (ΔG_k) barriers to cleave the C−C bond (eq 7), excluding the energy required to desorb 2 H* from the surface, in all ethane-derived intermediates on Pt(111) and other transition metals (Figure 4). The transition-state formation enthalpy (ΔH_k) is 229 kJ mol^{-1} for C−C bond cleavage in CH$_3$CH*, 14 kJ mol^{-1} lower than *CHCH* (243 kJ mol^{-1}) on Pt(111). These enthalpic barriers, however, do not reflect the increase in entropy associated with the formation of H$_2$(g) via C−H bond activations and H* atom desorption. This increase in entropy results in a decrease in free energy (eq 9), favoring C−C bond cleavage in more deeply dehydrogenated intermediates as those routes produce more H$_2$(g). Thus, *CH−CH* bond cleavage has the lowest free-energy barrier (197 kJ mol^{-1}) compared to 254 and 279 kJ mol^{-1} for *CH$_3$−CH* and CH$_3$−CH$_2$* bonds (Figure 4b), respectively. These entropic effects cannot offset the large increase in enthalpic barriers for *CH−C* and *C−C* activations; CH$_3$C* is the next most reactive intermediate (Figure 3b) after *CHCH* with a ΔG_k value of 231 kJ mol^{-1}. Figures 5 and 6 show the enthalpy and free-energy barriers for C−C bond cleavage in all intermediates relative to the transition state for *CHCH* ($\Delta \Delta H_k$ and $\Delta \Delta G_k$) for all examined metals. Similar to Pt and Ir, the free-energy barriers for *CH−CH* bond activation on Rh, Ru, and Os are far more favorable (by ≥51 kJ mol^{-1}) than the next most reactive intermediates. Cleaving the C−C bond in more saturated intermediates, however, start to compete with *CH−CH* activation as one moves to the right of the periodic table. On Ni and Pd, for example, CH$_3$CH* activation is only 39 and 12 kJ mol^{-1} less favorable than *CH−CH* activation, respectively (Figures 5b and 6). These data (Figures 4b, 5b, and 6) suggest that ethane hydrogenolysis on Group 8 and 9 metals (Ru, Os, Rh, and Ir in this work) occurs via C−C cleavage in *CHCH* intermediates; for Group 10 metals (Ni, Pd, and Pt in this work), the most favorable mechanism is also via C−C cleavage in *CHCH* intermediates, but other intermediates have activation free energies within 40 kJ mol^{-1}, indicating some uncertainty and that multiple routes may coexist on Group 10 metals at relevant conditions. Group 11 (coinage) metals (Cu, Ag, and Au) behave very differently than Groups 8−10. These coinage metals prefer to cleave the C−C bond in the most saturated intermediate CH$_3$CH$_2$* (Figure 4a) even after the inclusion of entropic effects associated with the formation of more H$_2$(g) molecules in more deeply dehydrogenated intermediates (Figure 4b); ΔG_k increases as intermediates dehydrogenate, and C−C activation of CH$_3$−CH$_2$* is more favorable than that of *CH−CH* by > 70 kJ mol^{-1} on coinage metals (Figures 5b and 6).

There is a clear trend between the metal group and the degree of saturation required for C−C bond cleavage (Figure 6); more noble metals, located on the right of the periodic table, prefer to cleave the C−C bond in the more hydrogenated intermediates than less noble metals. For Group 8 and 9 metals, activation via *CHCH* is preferred over other routes by an average of 69 kJ mol^{-1} and the second-most active routes involve similarly dehydrogenated intermediates (*CH$_2$CH* and *CHC*). On Group 10 metals, the average preference is 28 kJ mol^{-1} and the second-most active
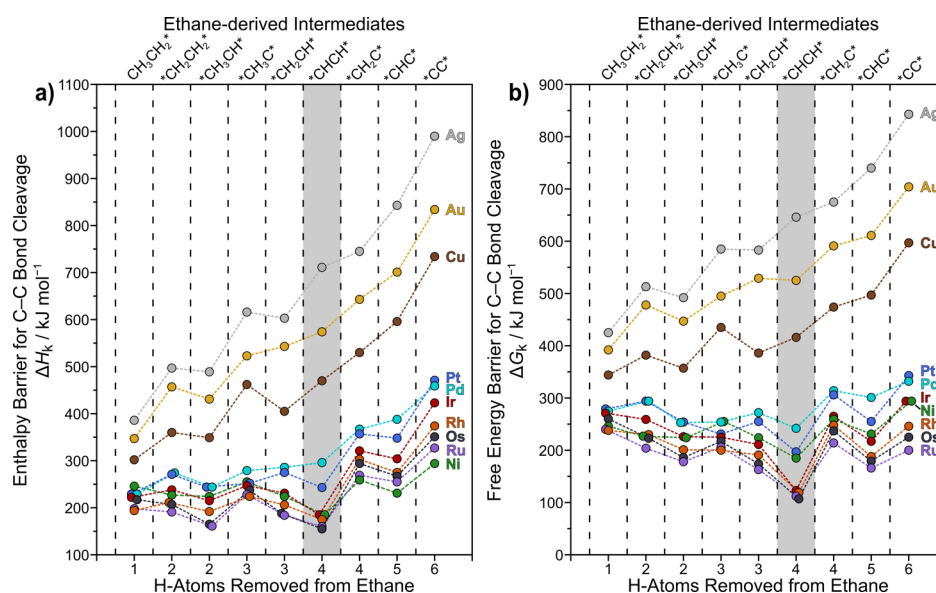

Figure 3. Transition-state structure for C−C bond cleavage in *CHCH* and the next most reactive intermediate on Pt (a,b) and Pd (c,d). Shown beneath images are ΔH_k and ΔG_k values (kJ mol^{-1}, eq 7, 593 K) and turnover rates (s^{-1}, eq 4, 593 K, 0.2 bar C$_2$H$_6$, 10 bar H$_2$). Important bond distances are shown in pm.

	Pt	*CH−CH*	*CH$_3$−C*
ΔH_k		243	252
ΔG_k		197	231
Rate		~10^{-9}	~10^{-11}

	Pd	*CH−CH*	*CH$_3$−CH*
ΔH_k		296	244
ΔG_k		242	253
Rate		~10^{-13}	~10^{-13}

two CH* fragments then form two CH$_4$ molecules through kinetically irrelevant hydrogenation steps (Step 1.5 in Scheme 1). This mechanism of C−C cleavage in *CHCH* intermediates ($y = 4$) at two sites ($\gamma = 2$) is consistent with previous studies on Ir(111) surfaces and Ir$_{119}$ half-particle models at low and high H* coverage.[23,35] The degree of H$_2$-inhibition ($\lambda = 3$, eqs 1 and 2) predicted from such a mechanism, however, is inconsistent with the measured λ value on 0.6 nm Pt clusters ($\lambda = 2.3$).[22] Measured λ values <3 on 0.6
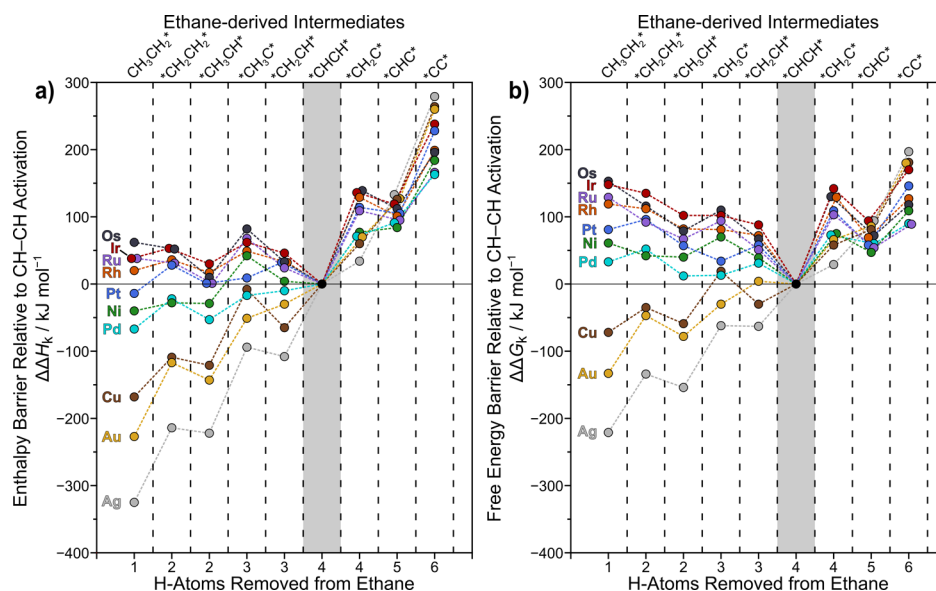
Figure 4. (a) Enthalpy ΔH_k and (b) free-energy ΔG_k barriers (eq 7) for C−C bond cleavage in ethane-derived intermediates on bare metal surfaces (593 K, 1 bar H_2).

Figure 5. (a) Enthalpy $\Delta\Delta H_k$ and (b) free-energy $\Delta\Delta G_k$ barriers for C−C bond activation in ethane-derived intermediates relative to the C−C bond activation barrier in *CHCH* (593 K, 1 bar H_2).


Figure 6. Ethane-derived intermediates with the lowest activation free-energy barrier relative to *CH−CH* bond activation ($\Delta\Delta G_k$) on examined metal surfaces. $\Delta\Delta G_k$ values are shown in kJ mol^{-1} (593 K, 1 bar H_2).

routes are in less-dehydrogenated species (*CH$_2$CH*, *CH$_3$CH*, and *CH$_3$C*). Finally, on Group 11 metals,

activation via *CHCH* is no longer preferred and, instead, activation via CH$_3$CH$_2$* is preferred by an average of 142 kJ mol^{-1}.

Notably, the range of activation barriers among examined metals decreases with increasing H-content in the reactive intermediate (Figure 4). For example, the free-energy barrier to cleave the C−C bond (ΔG_k, Figure 4b) in *CC* varies from 843 kJ mol^{-1} on Ag to 216 kJ mol^{-1} on Ru (a range of 627 kJ mol^{-1}), while ΔG_k values for CH$_3$−CH$_2$* bond activation varies from 425 to 240 kJ mol^{-1} on Ag and Ru (a range of 185 kJ mol^{-1}), respectively. Thus, the influence of the metal varies from 627 kJ mol^{-1} for C−C bond cleavage in the completely dehydrogenated *CC* species to only 185 kJ mol^{-1} for CH$_3$CH$_2$*. This follows from bond-order conservation principles[58] as C−H bonds are broken and C−M bonds are formed and/or strengthened, thus resulting in
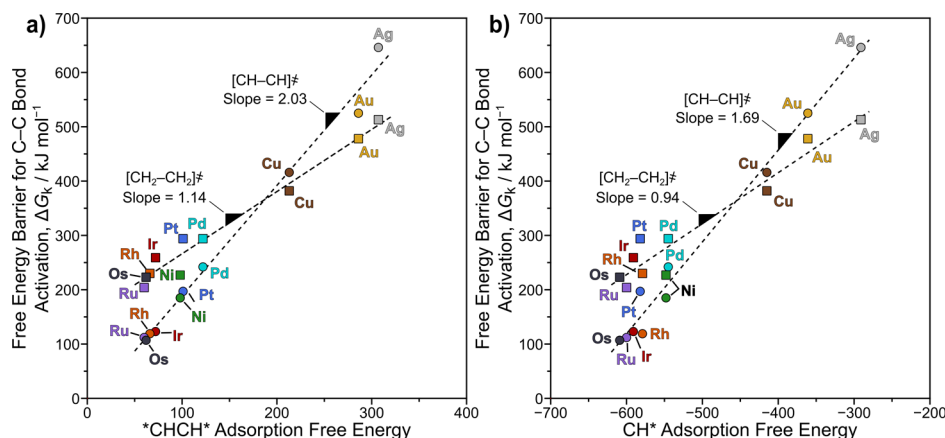
Figure 7. Free-energy barriers ΔG_k for C−C bond activation in *CHCH* (circles) and *CH$_2$CH$_2$* (squares) as a function of (a) *CHCH* and (b) CH* adsorption free energies (593 K, 1 bar H$_2$).

stronger effects of catalyst composition. These findings indicate that increasing the H-content in the reactive intermediate decreases the sensitivity of bond activation to the type of metal catalyst.

3.2. Brønsted−Evans−Polanyi Relation. Brønsted−Evans−Polanyi (BEP) or linear free-energy relationships[59−62] have been used in DFT studies[63−70] to correlate the activation energy of a reaction with the reactants, products, or atomic binding energies (descriptors) based on bond-order conservation principles.[58] Such correlations are developed by examining the relationship between activation barriers and various descriptors for a set of catalytic materials. These correlations can then be used to estimate activation barriers for many theoretical catalyst structures (typically alloys) using less computationally expensive calculations (optimizations of adsorbed species) in screening studies.[71] One of the most common applications for these bond-order conservation principles to heterogenous catalysis is the scaling relationships between N$_2$ dissociation barriers and N* binding energies for ammonia synthesis on metal surfaces proposed by Nørskov et al.[72−76] Here, we examine similar correlations for ethane hydrogenolysis on metal surfaces.

Figure 7 shows the transition-state formation free energies (ΔG_k) for *CH−CH* and *CH$_2$−CH$_2$* bond cleavage as a function of *CHCH* and CH* adsorption free energies. The adsorption free energy of *CHCH* more accurately predicts *CH−CH* bond activation barriers and the sequence of reactivity among examined metals (Figure 7a) compared to the CH* binding energy (Figure 7b) because the structure and atomic composition of *CHCH* more closely resemble the *CH−CH* transition state than CH*. The trend in *CHCH* adsorption free energy, however, does not accurately predict differences in activation barriers in other ethane-derived intermediates (e.g., *CH$_2$CH$_2$*, Figure 7a). Moreover, the slope decreases from 2.03 for *CH−CH* activation to 1.14 for *CH$_2$−CH$_2$* activation because increasing the H-content reduces the sensitivity to the catalyst identity, and coinage metals favor C−C bond activation in more saturated intermediates (CH$_3$−CH$_2$*). Although such linear correlations are useful for rapid screening analysis, their apparent accuracy is bolstered by the inclusion of nonreactive coinage metals; trends across Group 8−10 metals offer a significantly less predictive value. Ultimately, these relationships may be useful in the screening of thousands of potential catalysts but otherwise they should be avoided for smaller studies (≤∼100

catalyst surfaces) given the current availability of computational resources and the robust nature of transition-state search algorithms.

3.3. Effective Free-Energy Barriers and DFT-Predicted Rates. Next, we examine DFT-predicted turnover rates for C−C bond cleavage through each intermediate (eq 4, 593 K, 0.2 bar C$_2$H$_6$, 10 bar H$_2$). Previous studies have shown that H* covers the surfaces of Group 8−10 metals at ambient conditions (1 bar H$_2$, 300 K)[36,37,77−81] and at practical hydrogenolysis conditions (2−20 bar H$_2$, 593 K).[22,23,31,34] H*, however, is not expected to saturate coinage metals at chemisorption or C−C hydrogenolysis conditions.[82−87] Measured turnover rates at high H$_2$/alkane pressure ratios on Pt, Ir, Rh, and Ru show that chemisorbed H* is the most abundant surface intermediate (MASI),[22,23,31,34] and thus, turnover rates here are calculated using the effective free-energy barriers ($\Delta G^{\ddagger}$, eq 5); these $\Delta G^{\ddagger}$ values include the free energy to desorb γ H* atoms from a H*-covered surface to create vacant sites (ΔG_γ, eq 8) in addition to the free energy to form the C−C bond cleavage transition state (ΔG_k, eq 7). Using a H*-covered Ir half-particle model in our recent DFT study,[35] we showed that C−C bond cleavage in ethane requires the desorption of two terrace H* atoms ($\gamma = 2$) to minimize coadsorbate interactions. Therefore, we assume that two H* desorb ($\gamma = 2$) prior to ethane hydrogenolysis on Group 8−10 metals, and thus, ΔG_γ values at $\gamma = 2$ (Table S1, Supporting Information) were used to calculate $\Delta G^{\ddagger}$ and predict turnover rates for C−C bond cleavage in each C$_2$H$_{6-y}$* intermediate (Figure 8). We will revisit this assumption for Pt in Section 3.4 as measurements have indicated that it is less inhibited by H$_2$ than other metals and this may be caused by fewer H* desorbing during the formation of the *CH−CH* activation transition state.

Activation of *CH−CH* intermediates occurs with the highest turnover rates on Group 8 and 9 metals ($\lambda = 3$) by several orders of magnitude than turnover rates for C−C activation in other intermediates, indicating that C−C bond cleavage turnover rates reflect the reaction of a single dehydrogenated intermediate. For example, Ru cleaves the *CH−CH* bond with a rate of 8.9×10^{-2} s^{-1} compared to a turnover rate of 9.8×10^{-6} s^{-1} for C−C cleavage in all other ethane-derived intermediates combined (Figure 8). C−C cleavage in more saturated intermediates, however, becomes competitive with *CH−CH* bond activation for Group 10 metals; the *CH−CH* activation turnover rate is only 3
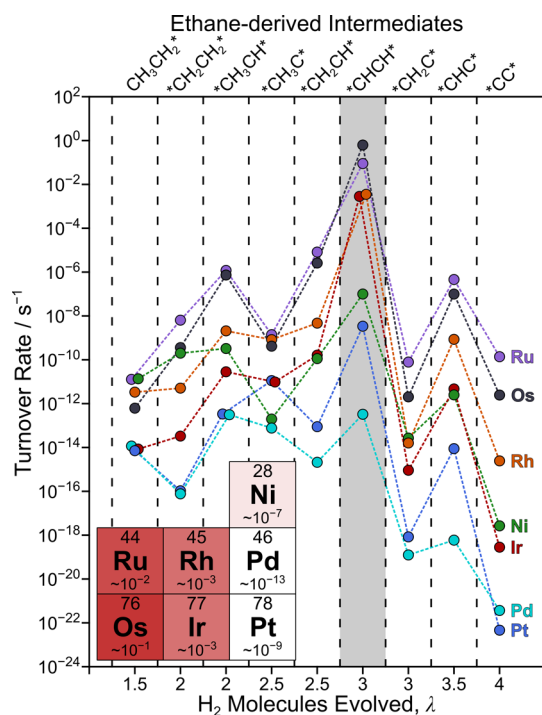
Figure 8. DFT-predicted turnover rates for C−C bond cleavage in each intermediate calculated using eq 4 (593 K, 0.2 bar C_2H_6, 10 bar H_2). The inset shows the turnover rate for CH−CH bond cleavage for each metal increasing from right (white) to left (red) in the periodic table. Turnover rates via different C−C bond cleavage intermediates and at different H_2 pressures are shown for each metal in the Supporting Information (Figure S10).

orders of magnitude higher than *CH$_3$−CH* and *CH$_3$−C* activations on Ni and Pt, respectively, and the rates of these two reactions are nearly identical to the *CH−CH* bond activation rate on Pd ($\sim 10^{-13}$ s^{-1}). These data indicate that for Group 10 metals, multiple reaction pathways are within the margin of error expected from DFT calculations, particularly for Pd catalysts, indicating that Pd catalysts may be less

inhibited by H_2 than Group 8 and 9 metals. Unfortunately, no n-alkane hydrogenolysis reaction kinetics have been measured on Pd catalysts at high H_2/alkane ratios, where surfaces would be H*-covered and thus comparable to other kinetic data described in this work on Ru, Rh, and Ir.

The total DFT-predicted ethane hydrogenolysis rates (sum of individual turnover rates for C−C bond cleavage in each intermediate) as a function of H_2 pressure are shown in Figure 9. DFT-predicted H_2-pressure dependencies were $[H_2]^{-3}$ ($\lambda = 3$) for metals except Pd, indicating that all ethane hydrogenolysis occurs via *CHCH* bond cleavage. For Pd, both *CH−CH* ($\lambda = 3$) and *CH$_3$CH* ($\lambda = 2$) intermediates (Figure 3c,d) contribute equally to the total rate giving an average λ value of 2.5. Total rates on Ru(001) and Rh(111) show a H_2-pressure dependence of $[H_2]^{-3}$ ($\lambda = 3$) and in quantitative agreement with the measured rates on 1.0 nm Ru and 0.9 nm Rh clusters that show a λ value of 3 and 3.1, respectively. Predicted rates on Ir(111) surfaces are $\sim$2 orders of magnitude higher than measured rates on 0.7 nm Ir particles but are in good agreement with measured rates on large 7 nm Ir clusters (Figure 9b), suggesting that C−C bond cleavage in ethane occurs preferentially on the (111) terrace sites on Ir; the (111) terrace sites dominate the surfaces of large metal clusters (>99% for 7 nm particles) and thus large particles closely resemble the Ir(111) periodic surface model. Measured turnover rates on 0.6 nm Pt, in contrast, are 2−3 orders of magnitude higher than predicted rates on Pt(111) surface and, critically, the measured λ value of 2.3 is inconsistent with the DFT-predicted value of 3.

These discrepancies between measured and DFT-predicted rates can be attributed to errors in DFT-predicted activation barriers calculated by the RPBE functional, which is expected to underestimate binding energies of adsorbed species[88] and thus underestimate overall free-energy barriers. Moreover, coadsorbate interactions between the transition state and coadsorbed H* atoms are neglected in these bare periodic surface models which may affect the stability of the transition state.[35] Although measured rates on small and large Ir clusters suggest that C−C bond cleavage occurs preferentially on
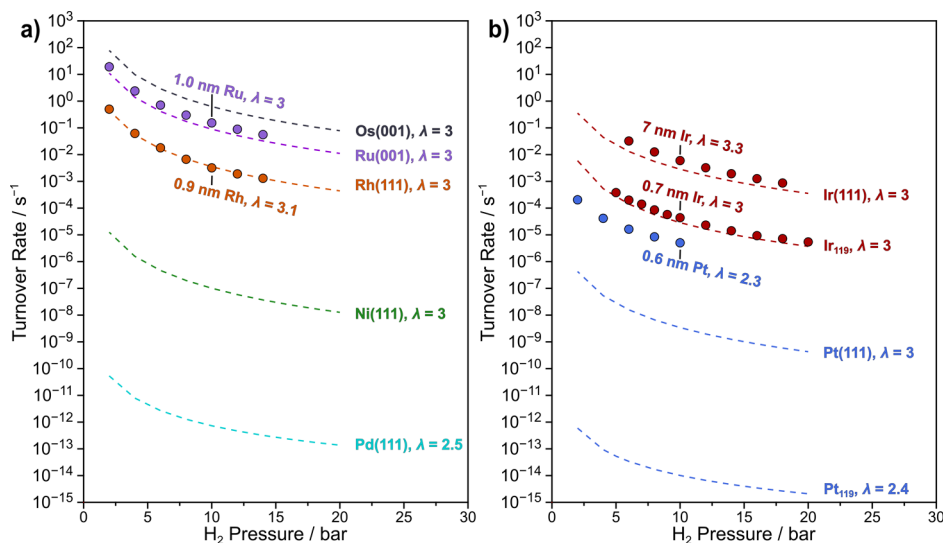
Figure 9. (a) Measured (circles) and DFT-predicted (dashed lines) hydrogenolysis rates as a function of H_2 pressure calculated using eq 4 (593 K, 0.2 bar C_2H_6) for Ru, Rh, Pd, and Os catalysts. (b) Predicted rates on bare Ir(111) and Pt(111) models as well as H*-covered Ir$_{119}$ and Pt$_{119}$ half-particle models. Measured rates are shown for 7 nm Ir, 0.7 nm Ir, 1.0 nm Ru, 0.6 nm Pt, and 0.9 nm Rh clusters.[22,23,31]
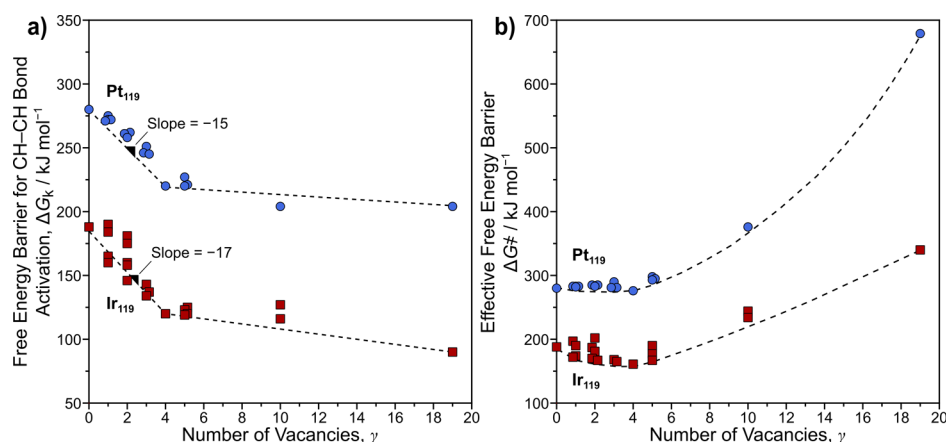
Figure 10. (a) Free energy to form the transition state [*CH−CH*] at vacant sites (ΔG_k) and (b) effective free-energy barriers for C−C bond activation in the *CHCH* intermediate as a function of the number of vacancies γ on H*-covered Ir$_{119}$ (past work)[35] and Pt$_{119}$ (this work) half-particles (593 K, 1 bar H$_2$). Multiple configurations of vacancies around the transition state have been examined at each γ value.

terrace sites on Ir,[22,23] low-coordinated sites (corners and edges) may have different effects on Pt and other metals and can cleave the C−C bond or alter the reactivity of terrace sites. Even if particle size effects on other metals are similar to those in Ir where low-coordinated sites are less reactive (i.e., blocked by H* or CH$_{0-3}$* species), the size of small metal particles is inaccurately estimated by H$_2$ chemisorption measurements as reported previously,[38] leading to inaccurate measured turnover rates because the fraction of terrace sites changes dramatically on small particles (<2 nm). Despite these discrepancies in measured and DFT-predicted turnover rates, the relative predicted rates among these metals and H$_2$-pressure dependencies (λ) are qualitatively consistent with the measured data (Figure 9).

The measured λ value (2.3) on Pt can only be attributed to a lower γ value (fewer than 2 H* atoms must be desorbed from the Pt surface because C−C bond cleavage via the *CHCH* intermediate is by far (a factor of 10^2, Figure 8) the most favorable pathway on the Pt(111) surface. Next, we use a H*-covered Pt$_{119}$ half-particle model to investigate the number of H* atoms that must be desorbed from Pt (γ) to cleave the *CH−CH* bond. The value of γ can be determined using DFT by modeling the reaction on H*-covered catalyst models to account for coadsorbate interactions, and the lateral relaxation of the adlayer allows curved nanoparticle models to more accurately predict these interactions than periodic surface models as shown in our previous study for the Ir catalyst.[35]

3.4. *CH−CH* Bond Cleavage on the H*-Covered Pt$_{119}$ Half-Particle. Site requirements for high-coverage surface reactions can be determined using DFT by varying the coverage of the MASI and analyzing this effect on the transition-state stability. In our recent study, however, we showed that periodic surface models fail in accurately accounting for coadsorbate interactions and predicting site requirements because of significant artifacts associated with their periodicity at high coverages.[35] The ability of curved nanoparticle models to relax the adlayer laterally leads to DFT-predicted turnover rates and site requirements consistent with measured data as shown for ethane hydrogenolysis on a H*-covered Ir$_{119}$ half-particle model (Figure 9b). This treatment, however, requires proper adjustments to DFT-predicted enthalpy and entropy of adsorbed species because the RPBE

functional and the harmonic oscillator approximations used here underestimate the enthalpy and entropy of adsorbed H* atoms, respectively.[54−57,88] Without any adjustments, the free energy required to desorb H* from Pt$_{119}$ terraces (ΔG_γ, eq 8) is negative (−28 kJ mol^{-1}, at 593 K and 1 bar H$_2$) and decreases by −22 kJ mol^{-1} H*$^{-1}$ (Table S2, Supporting Information), indicating that H* desorption from Pt is favorable at these conditions. At 300 K, ΔG_γ is also negative (−11 kJ mol^{-1}) and decreases by −4 kJ mol^{-1} H*$^{-1}$ (Table S3, Supporting Information), despite compelling experimental evidence in the literature demonstrating that hydrogen saturates Pt surfaces in H$_2$ chemisorption measurements at ambient conditions.[37,81,89−91] The DFT-estimated entropy of adsorbed H* (S[H*]) is near 15 J mol^{-1} K^{-1} at 593 K, far below reported values during high-temperature chemisorption experiments (∼60 J mol^{-1} K^{-1})[92] and values predicted by quantum and semi-classical treatments of a DFT-generated potential energy surface (PES) on Pt(100).[57] Moreover, previous studies have shown that the RPBE functional underestimates the adsorption enthalpy of H* by ∼10 kJ mol^{-1} because it neglects attractive dispersive interactions.[88] Therefore, S[H*] values were adjusted to give an average S[H*] of ∼60 J mol^{-1} K^{-1} at 593 K and the RPBE-estimated enthalpies were increased by 10 kJ mol^{-1} per H* atom, consistent with prior treatments.[35] These adjustments lead to positive ΔG_γ values that increase by 18 kJ mol^{-1} H*$^{-1}$ at 593 K and 21 kJ mol^{-1} H*$^{-1}$ at 300 K (Tables S2 and S3, Supporting Information), consistent with experimental observations.

We first analyze the free energy to form the *CH−CH* bond cleavage transition state at γ vacant sites (multiple configurations of vacancies have been examined) on the Pt$_{119}$ terrace excluding the free energy to form these vacancies (ΔG_k), to examine the effects of coadsorbate interactions between the transition state and coadsorbed H* atoms (Figure 10a). Here, we only consider *CH−CH* bond cleavage on the (111) terrace to exclude the direct effects of undercoordinated sites (corners and edges) and to make a comparison with the periodic Pt(111) surface. ΔG_k decreases rapidly from 280 kJ mol^{-1} at $\gamma = 0$ to 220 kJ mol^{-1} at $\gamma = 4$ with a slope of −15 kJ mol^{-1} γ^{-1} before it starts to decrease weakly to 204 kJ mol^{-1} at $\gamma = 19$ with a slope of −1 kJ mol^{-1} γ^{-1}. The dramatic change in slope at $\gamma = 4$ indicates strong repulsive interactions between the transition state and the vicinal 4 H* atoms because the

CH−CH transition state interacts with four metal atoms (Figure 3a). The slight decrease in slope at γ = 0−4 in Pt_{119} (-15 kJ mol^{-1} γ^{-1}) compared to Ir_{119} (-17 kJ mol^{-1} γ^{-1}), however, suggests that coadsorbate interactions are weaker on Pt. The reason for these weaker coadsorbate interactions on Pt_{119} is likely because Pt saturates at lower H* coverages than Ir. The Ir_{119} model has a H* coverage of 1.69 ML (3 H* on corner atoms, 2 H* on edge atoms, and 1 H* on terrace atoms), whereas Pt_{119} has a coverage of 1.30 ML (1 H* on corner atoms, 1 bridging H* between corner and edge atoms, and 1 H* on terrace atoms); thus, terrace H* atoms on Pt_{119} are more able to relax laterally and decrease repulsive interactions with the transition state.

Figure 10b shows the effective free-energy barrier ($\Delta G^{\ddagger}$) for *CH−CH* bond cleavage on Pt_{119}, that is, the energy to form the transition state (ΔG_k) in addition to the energy to desorb γ H* (ΔG_γ) as a function of γ. Although ΔG_k at γ = 4 (220 kJ mol^{-1}) is much lower than ΔG_k at γ = 0 (280 kJ mol^{-1}) on Pt_{119} (Figure 10a), the penalty to desorb H* from the surface renders $\Delta G^{\ddagger}$ constant (~280 kJ mol^{-1}) at γ = 0−4 before ΔG_γ prevails at $\gamma \geq 5$ (Figure 10b). $\Delta G^{\ddagger}$ values for Ir_{119} are lower than those for Pt_{119} because Ir is more reactive than Pt and change weakly at γ = 1−4 from 170 to 161 kJ mol^{-1}. Turnover rates, in addition to $\Delta G^{\ddagger}$, also depend inversely on H_2 pressure (eq 4) and thus increasing γ decreases the turnover rate. The total DFT-predicted turnover rates as a function of H_2 pressure on Pt_{119} decreases from 5.9 × 10^{-13} s^{-1} at 2 bar H_2 to 2.1 × 10^{-15} s^{-1} at 20 bar H_2 (Figure 9b) with H_2-pressure dependence of $[H_2]^{-2.4}$, while Ir_{119} shows a H_2-pressure dependence of $[H_2]^{-3}$. The H_2-pressure dependence indicates that *CH−CH* bond cleavage (y = 4) on Pt requires fewer vacant sites (γ = 0−1) than on Ir (γ = 2), leading to a λ value of 2.4 (eq 2), consistent with a measured value of 2.3 on 0.6 nm Pt clusters.[22] The discrepancy between the DFT-predicted rate on Pt_{119} and the measured rate on 0.6 nm Pt clusters, however, may indicate that *CH−CH* bond cleavage occurs on undercoordinated sites near the corners and edges of the particle instead of the (111) terrace examined in this study. These undercoordinated sites represent >85% of the surface of 0.6 nm clusters and they could be more reactive than the terrace sites because they are less saturated with H* in Pt compared to Ir.[38] The bare Pt(111) surface shows higher turnover rate compared to the H*-covered Pt_{119} (Figure 9b) because it lacks coadsorbate interactions, leading to lower ΔG_k values. Furthermore, H* binds more strongly on the (111) terrace of small particles compared to the (111) periodic surface models as reported previously,[38] and thus, the free energy to desorb H* from the Pt(111) surface (ΔG_γ) is also lower than on Pt_{119}. Despite the discrepancy between the predicted and measured turnover rates, the Pt_{119} half-particle model accurately predicts the mechanism and site requirements for ethane hydrogenolysis.

4. CONCLUSIONS

The effect of the type of metal catalyst on ethane hydrogenolysis mechanism was investigated using DFT. The calculated free-energy barriers indicate that C−C bond cleavage in ethane occurs predominantly via the *CHCH* intermediate for Group 8−10 metals (Ru, Os, Rh, Ir, Ni, and Pt) except for Pd, where the *CH$_3$CH* intermediate also contributes to the hydrogenolysis turnover rate. The preference toward cleaving the *CH−CH* bond decreases as one moves from left to right in the periodic table and cleaving the C−C bond in more hydrogenated intermediates starts to become more favorable. Coinage metals (Group 11: Cu, Ag, and Au) cleave the C−C bond in the most saturated intermediate (*CH$_3$CH$_2$*), suggesting that the metal catalyst becomes less effective and ethane hydrogenolysis proceeds via near-thermal activation of CH_3CH_3. Similar periodic table trends are also observed in DFT-predicted turnover rates, that is, less noble metals (left) are more active than more noble metals (right), consistent with measured turnover rates that decrease as Ru > Rh > Ir > Pt. Furthermore, the predicted turnover rates show a H_2-pressure dependence of $[H_2]^{-3}$ (λ = 3) for Group 8−10 metals, in agreement with the measured λ of ~3 for Ru, Rh, and Ir. Pd shows a λ value of 2.5 because both *CHCH* (λ = 3) and *CH$_3$CH* (λ = 2) intermediates contribute equally to the total turnover rate.

We were able to confirm, using a H*-covered Pt_{119} half-particle model, that Pt also cleaves the C−C bond in *CHCH* and the lower measured λ of 2.3 on 0.6 nm Pt clusters indicates that fewer H* atoms desorb from the H*-covered surface to accommodate the *CH−CH* transition state because H* saturates Pt surfaces at lower coverages than Ir as reported previously. Curved nanoparticle models, as shown previously, can relax the adlayer strains laterally and more accurately predict the number of vacant sites required for *CH−CH* bond activation. The lower H*-coverage in Pt increases the degree of adlayer relaxation, allowing *CH−CH* bond activation to occur at 0−1 vacant sites (γ = 0−1) and leading to a λ value of 2.4, consistent with the measured value of 2.3. This study provides insights into the effects of metals on the ethane hydrogenolysis mechanism and provides additional evidence for the accuracy of curved nanoparticle models in predicting coadsorbate interactions at high coverages.

■ ASSOCIATED CONTENT

⑤ Supporting Information

The Supporting Information is available free of charge on the ACS Publications website at DOI: 10.1021/acs.jpcc.8b11070.

> Details of DFT calculations, ΔG_γ values, and DFT-predicted turnover rates via different C−C bond cleavage intermediates and at different H_2 pressures (PDF)

■ AUTHOR INFORMATION

Corresponding Author
*E-mail: hibbitts@che.ufl.edu.

ORCID ⓘ
David Hibbitts: 0000-0001-8606-7000

Notes
The authors declare no competing financial interest.

■ ACKNOWLEDGMENTS

and proofreading from Alexander Hoffman and Steven Nystrom (University of Florida) are gratefully acknowledged.

■ REFERENCES

(1) Weitkamp, J.; Jacobs, P. A.; Martens, J. A. Isomerization and hydrocracking of C9 through C16 n-alkanes on Pt/HZSM-5 zeolite. *Appl. Catal.* **1983**, *8*, 123−141.

(2) McVicker, G.; Daage, M.; Touvelle, M. S.; Hudson, C. W.; Klein, D. P.; Baird, W. C., Jr; Cook, B. R.; Chen, J. G.; Hantzer, S.; Vaughan, D. W.; et al. Selective Ring Opening of Naphthenic Molecules. *J. Catal.* **2002**, *210*, 137−148.

(3) Do, P.; Alvarez, W.; Resasco, D. Ring Opening of 1,2- and 1,3-dimethylcyclohexane on Iridium Catalysts. *J. Catal.* **2006**, *238*, 477−488.

(4) Dokjampa, S.; Rirksomboon, T.; Phuong, D. T. M.; Resasco, D. E. Ring Opening of 1,3-dimethylcyclohexane on Ir Catalysts. *J. Mol. Catal. A: Chem.* **2007**, *274*, 231−240.

(5) Shi, H.; Gutiérrez, O. Y.; Haller, G. L.; Mei, D.; Rousseau, R.; Lercher, J. A. Structure sensitivity of hydrogenolytic cleavage of endocyclic and exocyclic C-C bonds in methylcyclohexane over supported iridium particles. *J. Catal.* **2013**, *297*, 70−78.

(6) Shi, H.; Li, X.; Haller, G. L.; Gutiérrez, O. Y.; Lercher, J. A. Active sites and reactive intermediates in the hydrogenolytic cleavage of C-C bonds in cyclohexane over supported iridium. *J. Catal.* **2012**, *295*, 133−145.

(7) Weisang, F.; Gault, F. G. Selective Isomerization of Methylpentanes on Iridium Catalysts. *J. Chem. Soc., Chem. Commun.* **1979**, 519−520.

(8) Speight, J. G. Petroluem Refinery Processes. In *Kirk-Othmer Encyclopedia of Chemical Technology*; Kirk, R. E., Seidel, A., Eds.; John Wiley and Sons Inc.: New Jersey, 2007; Vol. 19, pp. 1−49.

(9) Iglesia, E.; Reyes, S. C.; Madon, R. J.; Soled, S. L. Selectivity Control and Catalyst Design in the Fischer-Tropsch Synthesis: Sites, Pellets, and Reactors. *Advances in Catalysis*; Academic Press, 1993; Vol. 39, pp. 221−302.

(10) Bond, G. C. *Metal-Catalysed Reactions of Hydrocarbons*; Springer: New York, 2005.

(11) Witzke, M. E.; Almithn, A.; Coonrod, C. L.; Hibbitts, D. D.; Flaherty, D. W. Mechanisms and Active Sites for C-O Bond Rupture within 2-Methyltetrahydrofuran over Ni, Ni12P5, and Ni2P Catalysts. *ACS Catal.* **2018**, *8*, 7141−7157.

(12) Hibbitts, D.; Iglesia, E. Prevalence of Bimolecular Routes in the Activation of Diatomic Molecules with Strong Chemical Bonds (O2, NO, CO, N2) on Catalytic Surfaces. *Acc. Chem. Res.* **2015**, *48*, 1254−1262.

(13) Chia, M.; Pagán-Torres, Y. J.; Hibbitts, D.; Tan, Q.; Pham, H. N.; Datye, A. K.; Neurock, M.; Davis, R. J.; Dumesic, J. A. Selective Hydrogenolysis of Polyols and Cyclic Ethers over Bifunctional Surface Sites on Rhodium-rhenium Catalysts. *J. Am. Chem. Soc.* **2011**, *133*, 12675−12689.

(14) Greeley, J.; Mavrikakis, M. Competitive Paths for Methanol Decomposition on Pt(111). *J. Am. Chem. Soc.* **2004**, *126*, 3910−3919.

(15) Oyama, S. T.; Zhao, H.; Freund, H.-J.; Asakura, K.; Włodarczyk, R.; Sierka, M. Unprecedented Selectivity to the Direct Desulfurization (DDS) Pathway in a Highly Active FeNi Bimetallic Phosphide Catalyst. *J. Catal.* **2012**, *285*, 1−5.

(16) Wang, H.; Iglesia, E. Mechanism and Site Requirements of Thiophene Hydrodesulfurization Catalyzed by Supported Pt Clusters. *ChemCatChem* **2011**, *3*, 1166−1175.

(17) Wang, H.; Iglesia, E. Thiophene Hydrodesulfurization Catalysis on Supported Ru Clusters: Mechanism and Site Requirements for Hydrogenation and Desulfurization Pathways. *J. Catal.* **2010**, *273*, 245−256.

(18) Abu, I. I.; Smith, K. J. HDN and HDS of model compounds and light gas oil derived from Athabasca bitumen using supported metal phosphide catalysts. *Appl. Catal., A* **2007**, *328*, 58−67.

(19) Stinner, C.; Prins, R.; Weber, T. Formation, Structure, and HDN Activity of Unsupported Molybdenum Phosphide. *J. Catal.* **2000**, *191*, 438−444.

(20) Cimino, A.; Boudart, M.; Taylor, H. Ethane Hydrogenation-cracking on Iron Catalysts with and without Alkali. *J. Phys. Chem.* **1954**, *58*, 796−800.

(21) Morikawa, K.; Benedict, W. S.; Taylor, H. S. The Activation of Specific Bonds in Complex Molecules at Catalytic Surfaces. II. The Carbon-hydrogen and Carbon-carbon Bonds in Ethane and Ethane-d. *J. Am. Chem. Soc.* **1936**, *58*, 1795−1800.

(22) Flaherty, D. W.; Iglesia, E. Transition-state Enthalpy and Entropy Effects on Reactivity and Selectivity in Hydrogenolysis of N-alkanes. *J. Am. Chem. Soc.* **2013**, *135*, 18586−18599.

(23) Flaherty, D. W.; Hibbitts, D. D.; Gürbüz, E. I.; Iglesia, E. Theoretical and Kinetic Assessment of the Mechanism of Ethane Hydrogenolysis on Metal Surfaces Saturated with Chemisorbed Hydrogen. *J. Catal.* **2014**, *311*, 350−356.

(24) Cortright, R. D.; Watwe, R. M.; Spiewak, B. E.; Dumesic, J. A. Kinetics of Ethane Hydrogenolysis over Supported Platinum Catalysts. *Catal. Today* **1999**, *53*, 395−406.

(25) Cortright, R. D.; Watwe, R. M.; Dumesic, J. A. Ethane Hydrogenolysis over Platinum. *J. Mol. Catal. A: Chem.* **2000**, *163*, 91−103.

(26) Sinfelt, J. Catalytic Hydrogenolysis of Ethane over the Noble Metals of Group VIII. *J. Catal.* **1967**, *8*, 82−90.

(27) Hibbitts, D. D.; Flaherty, D. W.; Iglesia, E. Effects of Chain Length on the Mechanism and Rates of Metal-catalyzed Hydrogenolysis of N-alkanes. *J. Phys. Chem. C* **2016**, *120*, 8125−8138.

(28) Engstrom, J. R.; Goodman, D. W.; Weinberg, W. H. Hydrogenolysis of ethane, propane, n-butane, and neopentane on the (111) and (110)-(1.times.2) surfaces of iridium. *J. Am. Chem. Soc.* **1988**, *110*, 8305−8319.

(29) Bond, G. C.; Cunningham, R. H. Alkane Transformations on Supported Platinum Catalysts. *J. Catal.* **1997**, *166*, 172−185.

(30) Bond, G. C.; Slaa, J. C. Catalytic and structural properties of ruthenium bimetallic catalysts: effects of pretreatment on the behaviour of various RuAl2O3 catalysts in alkane hydrogenolysis. *J. Mol. Catal. A: Chem.* **1995**, *101*, 243−253.

(31) Flaherty, D. W.; Hibbitts, D. D.; Iglesia, E. Metal-catalyzed C-C Bond Cleavage in Alkanes: Effects of Methyl Substitution on Transition-state Structures and Stability. *J. Am. Chem. Soc.* **2014**, *136*, 9664−9676.

(32) Hibbitts, D. D.; Flaherty, D. W.; Iglesia, E. Role of Branching on the Rate and Mechanism of C-C Cleavage in Alkanes on Metal Surfaces. *ACS Catal.* **2015**, *6*, 469−482.

(33) Boudart, M.; Ptak, L. D. Reactions of Neopentane on Transition Metals. *J. Catal.* **1970**, *16*, 90−96.

(34) Flaherty, D. W.; Uzun, A.; Iglesia, E. Catalytic Ring Opening of Cycloalkanes on Ir Clusters: Alkyl Substitution Effects on the Structure and Stability of C-C Bond Cleavage Transition States. *J. Phys. Chem. C* **2015**, *119*, 2597−2613.

(35) Almithn, A.; Hibbitts, D. Effects of Catalyst Model and High Adsorbate Coverages in Ab Initio Studies of Alkane Hydrogenolysis. *ACS Catal.* **2018**, *8*, 6375−6387.

(36) Mcvicker, G.; Baker, R. K.; Garten, R. L.; Kugler, E. L. Chemisorption Properties of Iridium on Alumina Catalysts. *J. Catal.* **1980**, *65*, 207−220.

(37) Kip, B. Determination of Metal Particle Size of Highly Dispersed Rh, Ir, and Pt Catalysts by Hydrogen Chemisorption and EXAFS. *J. Catal.* **1987**, *105*, 26−38.

(38) Almithn, A. S.; Hibbitts, D. D. Supra-monolayer coverages on small metal clusters and their effects on H2 chemisorption particle size estimates. *AIChE J.* **2018**, *64*, 3109−3120.

(39) Kresse, G.; Furthmüller, J. Efficiency of Ab-initio Total Energy Calculations for Metals and Semiconductors Using a Plane-wave Basis Set. *Comput. Mater. Sci.* **1996**, *6*, 15−50.

(40) Kresse, G.; Furthmüller, J. Efficient iterative schemes forab initiototal-energy calculations using a plane-wave basis set. *Phys. Rev. B: Condens. Matter Mater. Phys.* **1996**, *54*, 11169−11186.

(41) Kresse, G.; Hafner, J. Ab initiomolecular dynamics for liquid metals. *Phys. Rev. B: Condens. Matter Mater. Phys.* **1993**, *47*, 558−561.

(42) Kresse, G.; Hafner, J. Ab initiomolecular-dynamics simulation of the liquid-metal-amorphous-semiconductor transition in germanium. *Phys. Rev. B: Condens. Matter Mater. Phys.* **1994**, *49*, 14251−14269.

(43) Blöchl, P. E. Projector Augmented-wave Method. *Phys. Rev. B: Condens. Matter Mater. Phys.* **1994**, *50*, 17953−17979.

(44) Kresse, G.; Joubert, D. From Ultrasoft Pseudopotentials to the Projector Augmented-wave Method. *Phys. Rev. B: Condens. Matter Mater. Phys.* **1999**, *59*, 1758−1775.

(45) Hammer, B.; Hansen, L. B.; Nørskov, J. K. Improved Adsorption Energetics Within Density-functional Theory Using Revised Perdew-Burke-Ernzerhof Functionals. *Phys. Rev. B: Condens. Matter Mater. Phys.* **1999**, *59*, 7413−7421.

(46) Perdew, J. P.; Burke, K.; Ernzerhof, M. Generalized Gradient Approximation Made Simple. *Phys. Rev. Lett.* **1996**, *77*, 3865−3868.

(47) Zhang, Y.; Yang, W. Comment on "Generalized Gradient Approximation Made Simple". *Phys. Rev. Lett.* **1998**, *80*, 890.

(48) Monkhorst, H. J.; Pack, J. D. Special Points for Brillouin-zone Integrations. *Phys. Rev. B: Solid State* **1976**, *13*, 5188−5192.

(49) Pack, J. D.; Monkhorst, H. J. "Special points for Brillouin-zone integrations"-a reply. *Phys. Rev. B: Solid State* **1977**, *16*, 1748−1749.

(50) Henkelman, G.; Jónsson, H. Improved Tangent Estimate in the Nudged Elastic Band Method for Finding Minimum Energy Paths and Saddle Points. *J. Chem. Phys.* **2000**, *113*, 9978−9985.

(51) Jónsson, H.; Mills, G.; Jacobsen, K. W. Nudged Elastic Band Method for Finding Minimum Energy Paths of Transitions. In *Classical and Quantum Dynamics in Condensed Phase Simulations*; Berne, B. J.; Ciccotti, G.; Coker, D. F., Eds.; World Scientific, 1998; pp. 385−404.

(52) Henkelman, G.; Jónsson, H. A Dimer Method for Finding Saddle Points on High Dimensional Potential Surfaces Using Only First Derivatives. *J. Chem. Phys.* **1999**, *111*, 7010−7022.

(53) Anslyn, E. V.; Dougherty, D. A. *Modern Physical Organic Chemistry*; University Science: Sausalito, CA, 2006.

(54) Campbell, C. T.; Sellers, J. R. V. The Entropies of Adsorbed Molecules. *J. Am. Chem. Soc.* **2012**, *134*, 18109−18115.

(55) Sprowl, L. H.; Campbell, C. T.; Árnadóttir, L. Hindered Translator and Hindered Rotor Models for Adsorbates: Partition Functions and Entropies. *J. Phys. Chem. C* **2016**, *120*, 9719−9731.

(56) Campbell, C. T.; Sprowl, L. H.; Árnadóttir, L. Equilibrium Constants and Rate Constants for Adsorbates: Two-Dimensional (2D) Ideal Gas, 2D Ideal Lattice Gas, and Ideal Hindered Translator Models. *J. Phys. Chem. C* **2016**, *120*, 10283−10297.

(57) Bajpai, A.; Mehta, P.; Frey, K.; Lehmer, A. M.; Schneider, W. F. Benchmark First-Principles Calculations of Adsorbate Free Energies. *ACS Catal.* **2018**, *8*, 1945−1954.

(58) Shustorovich, E. The Bond-Order Conservation Approach to Chemisorption and Heterogeneous Catalysis: Applications and Implications. *Advances in Catalysis*; Elsevier, 1990; Vol. 37, pp 101−163.

(59) Evans, M. G.; Polanyi, M. Inertia and Driving Force of Chemical Reactions. *Trans. Faraday Soc.* **1938**, *34*, 11.

(60) Bronsted, J. N. Acid and Basic Catalysis. *Chem. Rev.* **1928**, *5*, 231−338.

(61) Bell, R. P. The Theory of Reactions Involving Proton Transfers. *Proc. Roy. Soc. Lond. Math. Phys. Sci.* **1936**, *154*, 414−429.

(62) Bligaard, T.; Nørskov, J. K.; Dahl, S.; Matthiesen, J.; Christensen, C. H.; Sehested, J. The Brønsted-Evans-Polanyi relation and the volcano curve in heterogeneous catalysis. *J. Catal.* **2004**, *224*, 206−217.

(63) Abild-Pedersen, F.; Greeley, J.; Studt, F.; Rossmeisl, J.; Munter, T. R.; Moses, P. G.; Skúlason, E.; Bligaard, T.; Nørskov, J. K. Scaling Properties of Adsorption Energies for Hydrogen-containing Molecules on Transition-metal Surfaces. *Phys. Rev. Lett.* **2007**, *99*, 016105.

(64) Fernández, E. M.; Moses, P. G.; Toftelund, A.; Hansen, H. A.; Martínez, J. I.; Abild-Pedersen, F.; Kleis, J.; Hinnemann, B.; Rossmeisl, J.; Bligaard, T.; et al. Scaling Relationships for Adsorption Energies on Transition Metal Oxide, Sulfide, and Nitride Surfaces. *Angew. Chem., Int. Ed. Engl.* **2008**, *47*, 4683−4686.

(65) Salciccioli, M.; Chen, Y.; Vlachos, D. G. Density Functional Theory-Derived Group Additivity and Linear Scaling Methods for Prediction of Oxygenate Stability on Metal Catalysts: Adsorption of Open-Ring Alcohol and Polyol Dehydrogenation Intermediates on Pt-Based Metals. *J. Phys. Chem. C* **2010**, *114*, 20155−20166.

(66) Jones, G.; Studt, F.; Abild-Pedersen, F.; Nørskov, J. K.; Bligaard, T. Scaling Relationships for Adsorption Energies of C2 Hydrocarbons on Transition Metal Surfaces. *Chem. Eng. Sci.* **2011**, *66*, 6318−6323.

(67) Sutton, J. E.; Vlachos, D. G. Error Estimates in Semi-empirical Estimation Methods of Surface Reactions. *J. Catal.* **2013**, *297*, 202−216.

(68) Sutton, J. E.; Vlachos, D. G. Effect of errors in linear scaling relations and Brønsted-Evans-Polanyi relations on activity and selectivity maps. *J. Catal.* **2016**, *338*, 273−283.

(69) Wang, S.; Vorotnikov, V.; Sutton, J. E.; Vlachos, D. G. Brønsted-Evans-Polanyi and Transition State Scaling Relations of Furan Derivatives on Pd(111) and Their Relation to Those of Small Molecules. *ACS Catal.* **2014**, *4*, 604−612.

(70) Bukowski, B. C.; Greeley, J. Scaling Relationships for Molecular Adsorption and Dissociation in Lewis Acid Zeolites. *J. Phys. Chem. C* **2016**, *120*, 6714−6722.

(71) Greeley, J. Theoretical Heterogeneous Catalysis: Scaling Relationships and Computational Catalyst Design. *Annu. Rev. Chem. Biomol. Eng.* **2016**, *7*, 605−635.

(72) Logadottir, A.; Rod, T. H.; Nørskov, J. K.; Hammer, B.; Dahl, S.; Jacobsen, C. J. H. The Brønsted-Evans-Polanyi Relation and the Volcano Plot for Ammonia Synthesis over Transition Metal Catalysts. *J. Catal.* **2001**, *197*, 229−231.

(73) Dahl, S.; Logadottir, A.; Jacobsen, C. J. H.; Nørskov, J. K. Electronic Factors in Catalysis: The Volcano Curve and the Effect of Promotion in Catalytic Ammonia Synthesis. *Appl. Catal., A* **2001**, *222*, 19−29.

(74) Logadóttir, Á.; Nørskov, J. K. Ammonia Synthesis over a Ru(0001) Surface Studied by Density Functional Calculations. *J. Catal.* **2003**, *220*, 273−279.

(75) Hellman, A.; Baerends, E. J.; Biczysko, M.; Bligaard, T.; Christensen, C. H.; Clary, D. C.; Dahl, S.; van Harrevelt, R.; Honkala, K.; Jonsson, H.; et al. Predicting Catalysis: Understanding Ammonia Synthesis from First-principles Calculations. *J. Phys. Chem. B* **2006**, *110*, 17719−17735.

(76) Honkala, K.; Hellman, A.; Remediakis, I. N.; Logadottir, A.; Carlsson, A.; Dahl, S.; Christensen, C. H.; Nørskov, J. K. Ammonia Synthesis from First-principles Calculations. *Science* **2005**, *307*, 555−558.

(77) Goodwin, J. Characterization of Highly Dispersed Ru Catalysts by Chemisorption. *J. Catal.* **1981**, *68*, 227−232.

(78) Shen, X.; Garces, L.-J.; Ding, Y.; Laubernds, K.; Zerger, R. P.; Aindow, M.; Neth, E. J.; Suib, S. L. Behavior of H2 chemisorption on Ru/TiO2 surface and its application in evaluation of Ru particle sizes compared with TEM and XRD analyses. *Appl. Catal., A* **2008**, *335*, 187−195.

(79) Crucq, A.; Lienard, G.; Degols, L.; Frennet, A. Hydrogen Adsorption on Rh. *Appl. Surf. Sci.* **1983**, *17*, 79−96.

(80) Johansson, M.; Skúlason, E.; Nielsen, G.; Murphy, S.; Nielsen, R. M.; Chorkendorff, I. Hydrogen adsorption on palladium and palladium hydride at 1bar. *Surf. Sci.* **2010**, *604*, 718−729.

(81) Vannice, M. Direct measurements of heats of adsorption on platinum catalysts II. CO on Pt dispersed on SiO2, Al2O3, SiO2$z.sbnd;Al2O3, and TiO2. *J. Catal.* **1986**, *97*, 66−74.

(82) Iwai, H.; Fukutani, K.; Murata, Y. Behavior of Atomic Hydrogen on Au(001). *Surf. Sci.* **1996**, *357−358*, 663−666.

(83) Lee, G.; Plummer, E. W. Interaction of Hydrogen with the Ag(111) Surface. *Phys. Rev. B: Condens. Matter Mater. Phys.* **1995**, *51*, 7250−7261.

(84) Rasmussen, P. B.; Holmblad, P. M.; Christoffersen, H.; Taylor, P. A.; Chorkendorff, I. Dissociative Adsorption of Hydrogen on Cu(100) at Low Temperatures. *Surf. Sci.* **1993**, *287−288*, 79−83.

(85) Lucci, F. R.; Darby, M. T.; Mattera, M. F. G.; Ivimey, C. J.; Therrien, A. J.; Michaelides, A.; Stamatakis, M.; Sykes, E. C. H. Controlling Hydrogen Activation, Spillover, and Desorption with Pd-Au Single-Atom Alloys. *J. Phys. Chem. Lett.* **2016**, *7*, 480−485.

(86) Lucci, F. R.; Marcinkowski, M. D.; Lawton, T. J.; Sykes, E. C. H. H2 Activation and Spillover on Catalytically Relevant Pt-Cu Single Atom Alloys. *J. Phys. Chem. C* **2015**, *119*, 24351−24357.

(87) O'Brien, C. P.; Miller, J. B.; Morreale, B. D.; Gellman, A. J. The Kinetics of $H_2 - D_2$ Exchange over Pd, Cu, and PdCu Surfaces. *J. Phys. Chem. C* **2011**, *115*, 24221−24230.

(88) Wellendorff, J.; Silbaugh, T. L.; Garcia-Pintos, D.; Nørskov, J. K.; Bligaard, T.; Studt, F.; Campbell, C. T. A Benchmark Database for Adsorption Bond Energies to Transition Metal Surfaces and Comparison to Selected DFT Functionals. *Surf. Sci.* **2015**, *640*, 36−44.

(89) Norton, P. R.; Richards, P. J. The Heat of Adsorption of Hydrogen on Platinum. *Surf. Sci.* **1974**, *44*, 129−140.

(90) Norton, P. R.; Richards, P. J. Hydrogen Isotope Chemisorption and Equilibration on Platinum. *Surf. Sci.* **1974**, *41*, 293−311.

(91) Sen, B.; Vannice, M. A. The influence of platinum crystallite size on H2 and CO heats of adsorption and CO hydrogenation. *J. Catal.* **1991**, *130*, 9−20.

(92) Diéguez, M. G.; Hibbitts, D.; Iglesia, E. Hydrogen Chemisorption Isotherms on Pt Particles at Catalytic Temperatures: Langmuir and Two-Dimensional Gas Models Revisited. *J. Phys. Chem. C* **2019**, DOI: 10.1021/acs.jpcc.8b10877.